This article has been accepted for publication in a future issue of this journal, but has not been fully edited. Content may change prior to final publication. Citation information: DOI 10.1109/TBME.2019.2953732, IEEE Transactions on Biomedical Engineering

Improved Block Sparse Bayesian Learning Method Using K-Nearest Neighbor Strategy for Accurate Tumor Morphology Reconstruction in Bioluminescence Tomography

Lin Yin, Kun Wang, Tong Tong, Yu An, Hui Meng, Xin Yang, and Jie Tian, *Fellow, IEEE*

Abstract*—*Objective: **Bioluminescence tomography (BLT) is a non-invasive technique designed to enable three-dimensional (3D) visualization and quantification of viable tumor cells in living organisms. However, despite the excellent sensitivity and specificity of bioluminescence imaging (BLI), BLT is limited by the photon scattering effect and ill-posed inverse problem. If the complete structural information of a light source is considered when solving the inverse problem, reconstruction accuracy will be improved.** ***Methods:*** **This paper proposed a block sparse Bayesian learning method based on K-nearest neighbor strategy (KNN-BSBL), which incorporated several types of a priori information including sparsity, spatial correlations among neighboring points, and anatomical information to balance over-sparsity and morphology preservation in BLT. Furthermore, we considered the Gaussian weighted distance prior in a light source and proposed a KNN-GBSBL method to further improve the performance of KNN-BSBL.** ***Results:*** **The results of numerical simulations and *in vivo* glioma-bearing mouse experiments demonstrated that KNN-BSBL and KNN-GBSBL achieved superior accuracy for tumor spatial positioning and morphology reconstruction.** ***Conclusion:*** **The proposed method KNN-BSBL incorporated several types of a priori information is an efficient and robust reconstruction method for BLT.**

***Index Terms*—bioluminescence tomography, block sparse Bayesian learning, morphology recovery.**

I. Introduction

BIOLUMINESCENCE imaging (BLI) plays an increasingly significant role in pre-clinical small animal studies. As a non-invasive and non-ionizing imaging approach, BLI has been commonly applied to tumor observation and *in vivo* therapeutic evaluation [1]–[3]. BLI utilizes a charge-coupled device camera to detect the light emitted from luciferase-labeled tumor cells; thus, it is a highly specific and sensitive technique to detect viable tumor cells in living organisms [2], [4]. Numerous studies have investigated bioluminescence tomography (BLT), which employs three-dimensional (3D) reconstruction of bioluminescent sources to more accurately locate and quantify tumors compared with BLI [1], [2]. However, to convert the detected planar bioluminescence flux on the surface of an object into reconstructed 3D bioluminescent sources inside the object body, the inverse problem of BLT is a mathematically ill-posed problem [1]–[4]. In the last decade, various methods have been designed to achieve a more accurate solution, including designing effective solution strategies [5]–[8] and utilizing different a priori information [9]–[11].

Many researchers developed various solution strategies to improve the accuracy of reconstruction. Initially, L2-norm regularization (Tikhonov regularization) is commonly used owing to its convenience; however, the reconstructed light source suffers from over-smooth effects [12]. In general, the reconstructed light sources are considerably smaller than the total volume of the tumor-bearing animal in BLT, which is regarded to be sparsely distributed [9], [13]. Thus, various sparse algorithms have been proposed based on the theory of compressed sensing (CS), such as adopting a sparse regularization term (e.g. L0 and L1) [9], [13], using greedy strategies [6], or adopting a sparse Bayesian approach [5]. These algorithms have continuously improved the reconstruction accuracy of BLT.

In a priori information, the anatomical structure of the imaging object can be used to effectively improve the accuracy of BLT reconstruction [14]. In general, computed tomography (CT) or magnetic resonance imaging (MRI) is frequently conducted with BLI to offer anatomical structures [9], [15]. Therefore, the major organs of the imaging object can be segmented, and each organ is assumed to have the same optical property, but it is different from the others. Such a so-called "heterogeneous strategy" further increases the accuracy of the tumor 3D positioning [16]. Recently, several small animal studies were reported for visualizing the glioma morphology by using fluorescence molecular tomography (FMT) [17], [18]. They not only utilized the organ-level anatomical information (brain, skull, muscle, etc.), but also applied the segmented tu-

This work was supported by the Ministry of Science and Technology of China under Grant No. 2017YFA0205200, 2017YFA0700401, 2016YFC0103803, and 2016YFA0100902, the National Natural Science Foundation of China under Grants No. 61671449, 81227901, 81527805, and 81871442, and the Chinese Academy of Sciences under Grant No. GJJSTD20170004, KFJ-STS-ZDTP-059, YJKYYQ20180048, QYZDJ-SSW-JSC005, and XDBS01030200. (Lin Yin and Kun Wang contributed equally to this work.) (Corresponding author: Jie Tian).

L. Yin, K. Wang, T. Tong, Y. An, H. Meng, and X. Yang are with CAS Key Laboratory of Molecular Imaging, Institute Of Automation, Chinese Academy of Sciences, Beijing 100190, China, and with University of Chinese Academy of Sciences, Beijing 100049, China.

J. Tian is with CAS Key Laboratory of Molecular Imaging, Institute Of Automation, Chinese Academy of Sciences, Beijing 100190, China, with University of Chinese Academy of Sciences, Beijing 100049, China, and with the Beijing Advanced Innovation Center for Big Data-Based Precision Medicine, Beihang University, Beijing, 100191, China. (email: tian@ieee.org).

This article has been accepted for publication in a future issue of this journal, but has not been fully edited. Content may change prior to final publication. Citation information: DOI 10.1109/TBME.2019.2953732, IEEE Transactions on Biomedical Engineering

mor tissue from CT/MRI as a mandatory convergence domain for optical source reconstruction. Although such strong a priori indeed improved the accuracy in terms of both tumor location and morphology, the overdependence of tumor segmentation inevitably resulted in potential bias caused by the incorrect assumption that the true tumor is the same as the segmented tumor. However, this assumption is inapplicable in BLT, because the bioluminescent source is assumed to be the gold-standard reference of the tumor, rather than the segmented tumor from anatomical images. Furthermore, several previous studies indicated that incorporating other appropriate a priori information to design algorithms could help achieve a more accurate reconstruction. For example, Gao *et al*. proposed a method that incorporated Gaussian weighted Laplace prior regularization to achieve an accurate glioma morphology recovery in BLT [19]. Chen *et al*. adopted structured sparsity prior regularization of the light source in diffuse optical tomography (DOT) [20], whereas Jiang *et al*. applied this prior regularization in their LASSO methods for fluorescence molecular tomography (FMT) [11], [21]. These studies helped improve the reconstruction quality by incorporating a priori information.

Recent studies have demonstrated that effective Bayesian reconstruction algorithms combined with a priori information can further improve reconstruction accuracy. Feng *et al*. used a hierarchal Bayesian approach to formulate hyperprior models and obtained improved reconstruction results for BLT [5]. Zhang *et al*. constructed a structural prior model for the inverse problem that improved FMT reconstruction quality based on the Bayesian framework [22]. Their studies explored a method to combine effective a priori information based on the characteristics of light source and anatomical structure with Bayesian theory to design efficient reconstruction algorithms, which provided us with a research direction.

In traditional signal processing field, Zhang *et al*. proposed a block sparse Bayesian learning (BSBL) algorithm, considerably improving the recovery performance of block sparse signals [23], which provided a new idea for BLT reconstruction. Inspired by BSBL algorithm, neighboring points of the light source were found to have the same or similar intensity distribution in BLT, which can be considered as a clustered distribution. Therefore, this paper proposed a block sparse Bayesian learning algorithm based on the K-nearest neighbor (KNN) strategy (KNN-BSBL) to achieve an accurate BLT reconstruction. We designed a block sparse prior model utilizing the spatial correlations among neighboring points based on the KNN strategy and used BSBL framework to solve the inverse problem for BLT. Furthermore, we incorporated Gaussian weighted distance prior [19] to improve intra-block correlation matrix and proposed an improved algorithm KNN-GBSBL. The performance of the KNN-BSBL and KNN-GBSBL was evaluated using numerical simulations and *in vivo* experiments, which were designed to assess the accuracy of tumor positioning and morphological reconstruction. The experimental results demonstrated that KNN-BSBL could achieve excellent spatial positioning and morphological reconstruction, and the performance of KNN-GBSBL was improved compared with KNN-BSBL.

The remainder of the paper is structured as follows: Section II presents the details of KNN-BSBL and KNN-GBSBL method for BLT reconstruction. Section III presents the numerical simulations and *in vivo* experiments used to compare and validate the different approaches. Section IV discusses the results and we conclude this study in Section V.

II. Method

BLT models the bioluminescent source distribution $\mathbf{x} \in \mathbb{R}^{N\times 1}$ and the luminescent flux on the surface of an object $\mathbf{\Phi} \in \mathbb{R}^{M\times 1}$ as a linear relationship according to the photon propagation theory [24], [25], as presented in Section A of the supplementary material:

$$\mathbf{A}\mathbf{x} = \mathbf{\Phi} + \mathbf{v}, \tag{1}$$

where $\mathbf{v} \in \mathbb{R}^{M\times 1}$ is an unknown error vector caused by data collection and processing. $\mathbf{A} \in \mathbb{R}^{M\times N}$ is the system matrix.

The maximum a posteriori (MAP) estimation of $\mathbf{x}$ based on the Bayesian theorem can be used to solve the inverse problem (1), which can be expressed as [26]

$$\begin{aligned}\hat{\mathbf{x}}_{\text{MAP}} &= \arg\max_{\mathbf{x}}\{\log p(\mathbf{x}|\mathbf{\Phi})\} \\ &= \arg\max_{\mathbf{x}}\{\log p(\mathbf{\Phi}|\mathbf{x}) + \log p(\mathbf{x})\},\end{aligned} \tag{2}$$

where $p(\mathbf{x}|\mathbf{\Phi})$ denotes the posteriori probability of the unknown source $\mathbf{x}$ given the measured $\mathbf{\Phi}$, $p(\mathbf{\Phi}|\mathbf{x})$ is the data likelihood (measurement model), and $p(\mathbf{x})$ is the priori probability (prior model) for the source $\mathbf{x}$.

A. KNN-BSBL algorithm

The design of the prior model is the most significant part under the Bayesian framework, which can incorporate a priori information to constrain the inverse problem and further improve the reconstruction quality [27]. As the light source in BLT is sparsely distributed and the neighboring points tend to have the same or similar intensity distribution, we proposed a block sparse Bayesian learning algorithm based on the K-nearest neighbor (KNN) strategy (KNN-BSBL). BLT data processing should utilize a finite element method (FEM) to discretize the CT data into a grid. However, this discretization is unordered and does not exhibit continuous correlation that occurs in signals; thus, the traditional BSBL algorithm cannot be directly applied to solve the BLT problem. Thereby, we designed a block sparse prior model based on the KNN strategy as shown in Fig. 1. The points on the grid have 3D spatial coordinates, and the value of $\mathbf{x}$ corresponds to the energy of each point. To explain the prior model more directly, we used $x_i (i = 1, \cdots, N)$ to represent i-th point on the grid and it was regarded as a center point. The KNN algorithm [28] was used to identify the nearest K points of the center point based on the spatial distance. In this manner, each x_i can be expanded to a group $\widetilde{\mathbf{x}}_i \in \mathbb{R}^{K\times 1}, i = 1, \cdots, N$; hence, the following calculations are based on groups instead of points. Finally, every center point x_i is obtained as follows:

$$x_i = \frac{\text{sum}(\widetilde{\mathbf{x}}_i)}{K}. \quad i = 1, \cdots, N \tag{3}$$

This article has been accepted for publication in a future issue of this journal, but has not been fully edited. Content may change prior to final publication. Citation information: DOI 10.1109/TBME.2019.2953732, IEEE Transactions on Biomedical Engineering

This prior model converts individual points in the light source $\mathbf{x}$ into the mean values of their neighbors. Thus, it reduces the sparsity of the Bayesian model during the inverse calculation to solve (1), which ultimately improves the reconstruction accuracy.

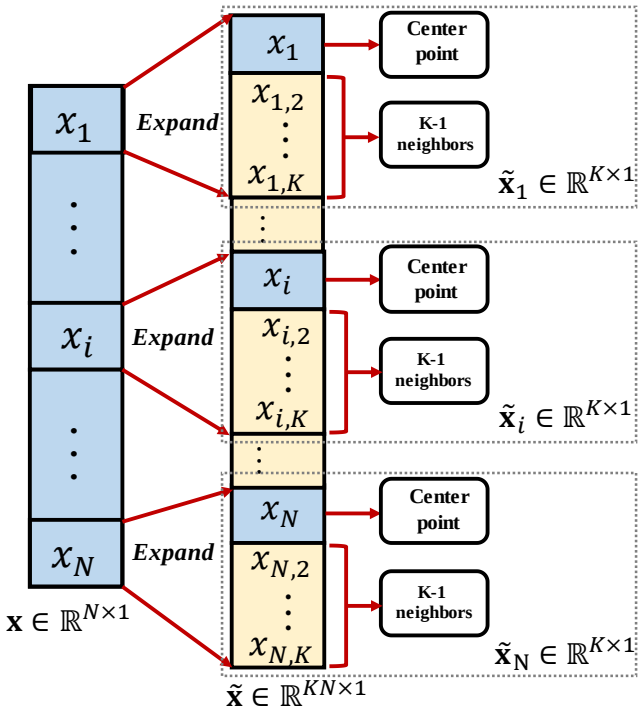

Fig. 1. Block sparse prior model establishment process. The vector $\mathbf{x}$ on the left represents the points on the grid. Based on the coordinates of these points, every point x_i is regarded as a center point and can be expanded into a group of K points using the KNN strategy.

Under BSBL framework, it assumes that each block $\widetilde{\mathbf{x}}_i \in \mathbb{R}^{K\times 1}$ satisfies a parameterized multivariate Gaussian distribution [29]:

$$\widetilde{\mathbf{x}}_i \sim \mathcal{N}(\mathbf{0}, \gamma_i \mathbf{B}_i), \quad i = 1, \cdots, N \tag{4}$$

where γ_i denotes a non-negative parameter that controls the sparsity of $\widetilde{\mathbf{x}}$ (when $\gamma_i = 0$, $\widetilde{\mathbf{x}}_i$ becomes zero) and $\mathbf{B}_i \in \mathbb{R}^{K\times K}$ is a positive definite and symmetric matrix, which is used to capture the correlation structure of the i-th block. Furthermore, it is assumed that the blocks $\widetilde{\mathbf{x}}$ satisfies a Gaussian distribution $\widetilde{\mathbf{x}} \sim \mathcal{N}(\mathbf{0}, \mathbf{\Sigma}_0)$, where

$$\mathbf{\Sigma}_0 = \mathrm{diag}\{\gamma_1 \mathbf{B}_1, \cdots, \gamma_N \mathbf{B}_N\}. \tag{5}$$

The error vector $\mathbf{v}$ can be modeled as an independent Gaussian distribution with zero mean and variance λ; i.e., $\mathbf{v} \sim \mathcal{N}(\mathbf{0}, \lambda \mathbf{I})$, which is used as measurement model in the Bayesian framework.

Therefore, the posteriori probability function on the parameters is obtained by combining the measurement and prior models within Bayes' rule [30]:

$$p(\widetilde{\mathbf{x}}|\mathbf{\Phi}; \lambda, \{\gamma_i \mathbf{B}_i\}_{i=1}^N) = \frac{p(\mathbf{\Phi}|\widetilde{\mathbf{x}}; \lambda) p(\widetilde{\mathbf{x}}; \{\gamma_i \mathbf{B}_i\}_{i=1}^N)}{\int p(\mathbf{\Phi}|\widetilde{\mathbf{x}}; \lambda) p(\widetilde{\mathbf{x}}; \{\gamma_i \mathbf{B}_i\}_{i=1}^N) \mathrm{d}\widetilde{\mathbf{x}}}, \tag{6}$$

where $p(\mathbf{\Phi}|\widetilde{\mathbf{x}}; \lambda)$ is a multivariate Gaussian likelihood corresponding to the measurement model and $p(\widetilde{\mathbf{x}}; \{\gamma_i \mathbf{B}_i\}_{i=1}^N)$ is the priori probability on the parameters:

$$p(\mathbf{\Phi}|\widetilde{\mathbf{x}}; \lambda) = (2\pi\lambda)^{-M/2} \exp\{-\|\mathbf{\Phi} - \mathbf{A}\mathbf{x}\|^2/(2\lambda)\}. \tag{7}$$

$$p(\widetilde{\mathbf{x}}; \{\gamma_i \mathbf{B}_i\}_{i=1}^N) = (2\pi)^{-\frac{N}{2}} \prod_{i=1}^{N} (\gamma_i \mathbf{B}_i)^{-\frac{1}{2}} \exp(-\frac{(\gamma_i \mathbf{B}_i)^{-1} \widetilde{\mathbf{x}}_i^2}{2}). \tag{8}$$

Therefore, the posteriori probability distribution is Gaussian $\mathcal{N}(\boldsymbol{\mu}, \mathbf{\Sigma})$ with [23], [30]

$$\mathbf{\Sigma} = (\mathbf{\Sigma}_0^{-1} + \lambda^{-1} \widetilde{\mathbf{A}}^T \widetilde{\mathbf{A}})^{-1}, \tag{9}$$

$$\boldsymbol{\mu} = \lambda^{-1} \mathbf{\Sigma} \widetilde{\mathbf{A}}^T \mathbf{\Phi}, \tag{10}$$

where $\widetilde{\mathbf{A}} \in \mathbb{R}^{M\times KN}$ denotes the expanded system matrix that comprises the corresponding columns of the expanded $\widetilde{\mathbf{x}}$. $\widetilde{\mathbf{A}}^T$ represents the transpose of $\widetilde{\mathbf{A}}$. Once the parameters $\lambda, \{\gamma_i, \mathbf{B}_i\}_{i=1}^N$ are estimated, the MAP estimate of $\widetilde{\mathbf{x}}$ can be directly obtained from the mean of the posterior:

$$\widetilde{\mathbf{x}}_{\mathrm{MAP}} = \arg\max_{\widetilde{\mathbf{x}}} \{\log p(\widetilde{\mathbf{x}}|\mathbf{\Phi}; \lambda, \{\gamma_i \mathbf{B}_i\}_{i=1}^N)\} = \boldsymbol{\mu}^*, \tag{11}$$

where $\boldsymbol{\mu}^*$ represents the mean of the posterior obtained after the parameters have been estimated. To estimate the parameters, we can obtain the cost function [30]:

$$\begin{aligned} \mathcal{L}(\Theta) &= 2\log \int p(\mathbf{\Phi}|\widetilde{\mathbf{x}}; \lambda) p(\widetilde{\mathbf{x}}; \{\gamma_i \mathbf{B}_i\}_{i=1}^N) \mathrm{d}\widetilde{\mathbf{x}} \\ &= -\log|\mathbf{h}| - \mathbf{\Phi}^T \mathbf{h}^{-1} \mathbf{\Phi}, \end{aligned} \tag{12}$$

where Θ denotes all parameters to be estimated: $\lambda, \{\gamma_i, \mathbf{B}_i\}_{i=1}^N$ and $\mathbf{h}$ is defined as $\mathbf{h} = \lambda \mathbf{I} + \widetilde{\mathbf{A}} \mathbf{\Sigma}_0 \widetilde{\mathbf{A}}^T$. A type-II maximum likelihood procedure can be used to estimate these parameters to maximize (12) [31], which can be implemented via the expectation maximization (EM) method [30], thereby obtaining the learning rules for the parameters.

$$\gamma_i \leftarrow \frac{1}{K} \mathrm{Tr}[\mathbf{B}_i^{-1} (\mathbf{\Sigma}_i + \boldsymbol{\mu}_i (\boldsymbol{\mu}_i)^T)], \quad i = 1, \cdots, N \tag{13}$$

$$\mathbf{B} \leftarrow \frac{1}{N} \sum_{i=1}^{N} \frac{\mathbf{\Sigma}_i + \boldsymbol{\mu}_i (\boldsymbol{\mu}_i)^T}{\gamma_i}, \tag{14}$$

$$\lambda \leftarrow \frac{\|\mathbf{\Phi} - \widetilde{\mathbf{A}} \boldsymbol{\mu}\|_2^2 + \sum_{i=1}^{N} \mathrm{Tr}(\mathbf{\Sigma}_i (\widetilde{\mathbf{A}}_i)^T \widetilde{\mathbf{A}}_i)}{M}. \tag{15}$$

Here, $\widetilde{\mathbf{A}}_i \in \mathbb{R}^{M\times K}$ represents a submatrix of the expanded system matrix that corresponds to $\widetilde{\mathbf{x}}_i$ and $\boldsymbol{\mu}_i$ and $\mathbf{\Sigma}_i$ denote the mean vector and variance matrix of the i-th block, respectively.

The points of a block can be modeled as a first-order auto-regressive process according to the BSBL algorithm, which is sufficient for modeling the intra-block correlation for several

This article has been accepted for publication in a future issue of this journal, but has not been fully edited. Content may change prior to final publication. Citation information: DOI 10.1109/TBME.2019.2953732, IEEE Transactions on Biomedical Engineering

applications [23]. In this case, the corresponding correlation matrix is a Toeplitz matrix with the following form:

$$\hat{\mathbf{B}} \triangleq \text{Toeplitz}([1, r, \ldots, r^{K-1}]) = \begin{bmatrix} 1 & r & r^2 & \ldots & r^{K-1} \\ r & 1 & r & \ldots & r^{K-2} \\ \vdots & \vdots & \ddots & & \vdots \\ r^{K-1} & r^{K-2} & \ldots & & 1 \end{bmatrix} \tag{16}$$

where $r = \text{sign}(\frac{m_1}{m_0})\min\{|\frac{m_1}{m_0}|, 0.99\}$, where m_0 and m_1 are the average of the elements along the main diagonal and main sub-diagonal of the matrix $\mathbf{B}$ in (14), respectively. 0.99 is an upper bound to ensure that r has a reasonable value [23]. All blocks are constrained to have the same correlation structure $\mathbf{B}_i = \hat{\mathbf{B}}(\forall i)$ under the BSBL framework [23], [30].

The learning rule for γ_i is the main body under the BSBL framework. However, it is computationally inefficient to use the EM algorithm to calculate γ_i. Therefore, Zhang *et al.* subsequently proposed a faster γ_i learning rule based on the bound optimization method [23], which also exhibited satisfactory performance. This learning rule is given as follows:

$$\gamma_i \leftarrow \sqrt{\frac{\widetilde{\mathbf{x}}_i^T \mathbf{B}_i^{-1} \widetilde{\mathbf{x}}_i}{\text{Tr}((\widetilde{\mathbf{A}}_i)^T (\mathbf{h}^*)^{-1} \widetilde{\mathbf{A}}_i \mathbf{B}_i)}}, \tag{17}$$

where $\mathbf{h}^* = \lambda \mathbf{I} + \widetilde{\mathbf{A}} \boldsymbol{\Sigma}_0^* \widetilde{\mathbf{A}}^T$ and $\boldsymbol{\Sigma}_0^* \triangleq \boldsymbol{\Sigma}_0|_{\gamma=\gamma^*}$ (γ^* is given in advance). The value of λ considerably affects the accuracy of the results, but the learning rule (15) is not robust [32]. In practice, λ is commonly treated as a regularizer and is assigned specific values [33]. A flow chart of KNN-BSBL is shown in Algorithm 1.

B. KNN-GBSBL algorithm

Under the KNN-BSBL framework, every block is assumed to have the same correlated structure $\mathbf{B}_i = \hat{\mathbf{B}}$, and $\mathbf{B}_i$ only affects the local convergence [23]. Therefore, the performance of the algorithm can be improved by imposing various constraints on the form of $\mathbf{B}_i$ [23]. In the field of FEM, discrete points on a grid are strongly correlated in terms of their spatial position. Thus, the correlation in a block is assumed to be inversely proportional to the Gaussian weighted distance between the center point and its neighbors [19]. Therefore, we proposed an improved algorithm KNN-GBSBL for calculating $\mathbf{B}_i$ in advance based on Gaussian weighted distance prior strategy, which simplifies the calculation process and enhances the performance. This was opted instead of learning it based on (14) and (16). $\mathbf{B}_i$ was defined as follows [19], [23]:

$$\mathbf{B}_i = \text{Toeplitz}(\mathbf{b}_{i,:}), \quad i = 1, \cdots, N \tag{18}$$

with

$$b_{i,j} = \begin{cases} 1, & i = j; \\ \exp(\frac{-d_{i,j}^2}{4R^2}), & i, j \in S_k, j \in U(i), i \neq j; \\ 0, & \text{otherwise.} \end{cases} \tag{19}$$

where $U(i)$ and S_k denote the neighborhood of point x_i and the points set of k-th property under FEM framework, respectively. Furthermore, R is the radius of the Gaussian kernel, and it is determined as detailed in [19]. $d_{i,j}$ is the Euclidean distance between x_i and x_j.

A flow chart of KNN-GBSBL is shown in Algorithm 2.

Algorithm 1 Algorithm flow of KNN-BSBL

Input: $\mathbf{A}$, $\boldsymbol{\Phi}$, λ; The group size K; The maximum number of iterations $T = 10$.
Output: The light source $\mathbf{x}$;

Initialize: $\widetilde{\mathbf{x}}^0 = \mathbf{0}$, $\boldsymbol{\Sigma}_0^i = \text{eye}(K)(\forall i)$, $\boldsymbol{\gamma} = \text{ones}(N, 1)$, $t = 0$.
Find the K neighbors of every center point x_i $(i = 1, \cdots, N)$ using KNN algorithm.
while 1 **do**
  $t = t + 1$;
  for $i = 1$ to N **do**
    Compute $\boldsymbol{\Sigma}_i$ and $\boldsymbol{\mu}_i$ based on (9) and (10);
    Compute the correlation matrix $\mathbf{B}$ using (14);
  end for
  Compute $\hat{\mathbf{B}}$ using (16)
  for $i = 1$ to N **do**
    $\mathbf{B}_i = \hat{\mathbf{B}}$;
    Compute γ_i using (17);
    Compute $\boldsymbol{\Sigma}_0^i$ based on (5);
  end for
  Compute $\widetilde{\mathbf{x}}^t$ using (11).
  if $t \geqslant T$ or $\|\widetilde{\mathbf{x}}^t - \widetilde{\mathbf{x}}^{t-1}\|_2 < 10^{-8}$ **then**
    break;
  end if
end while
Return the distribution of $\mathbf{x}$ according to (3), and also consider non-negative constraint of $\mathbf{x}$.

Algorithm 2 Algorithm flow of KNN-GBSBL

Input: $\mathbf{A}$, $\boldsymbol{\Phi}$, λ; The group size K; The maximum number of iterations $T = 10$.
Output: The light source $\mathbf{x}$;

Initialize: $\widetilde{\mathbf{x}}^0 = \mathbf{0}$, $\boldsymbol{\Sigma}_0^i = \text{eye}(K)(\forall i)$, $\boldsymbol{\gamma} = \text{ones}(N, 1)$, $t = 0$.
Find the K neighbors of every center point x_i $(i = 1, \cdots, N)$ using KNN algorithm.
Compute the correlation matrix $\mathbf{B}_i$ $(i = 1, \cdots, N)$ under (18) and (19)
while 1 **do**
  $t = t + 1$;
  for $i = 1$ to N **do**
    Compute $\boldsymbol{\Sigma}_i$ and $\boldsymbol{\mu}_i$ based on (9) and (10);
    Compute γ_i using (17);
    Compute $\boldsymbol{\Sigma}_0^i$ based on (5);
  end for
  Compute $\widetilde{\mathbf{x}}^t$ based on (11).
  if $t \geqslant T$ or $\|\widetilde{\mathbf{x}}^t - \widetilde{\mathbf{x}}^{t-1}\|_2 < 10^{-8}$ **then**
    break;
  end if
end while
Return the distribution of $\mathbf{x}$ according to (3), and also consider non-negative constraint of $\mathbf{x}$.

This article has been accepted for publication in a future issue of this journal, but has not been fully edited. Content may change prior to final publication. Citation information: DOI 10.1109/TBME.2019.2953732, IEEE Transactions on Biomedical Engineering

III. Experiments and Results

In this section, the digital mouse simulations [34] and *in vivo* glioma-bearing mice experiments were designed to evaluate the BLT reconstruction performance of KNN-BSBL and KNN-GBSBL. Two existing algorithms for BLT were used for comparison: SBR (sparse Bayesian method) and GWLP (deformed L2 method). Because glioma is a typical intracranial tumor and only invades the brain, we used the feasible region, which was limited inside the brain for all methods [19]. Furthermore, because the value of the points outside the feasible region is zero, KNN strategy was used based on the points in the feasible region. All programs were run on a computer with an Intel(R) Core(TM) i7-6700 CPU (3.40 GHz) and 16-GB RAM.

A. Numerical Simulations

In numerical simulations, we used a head of a mouse atlas as shown in Fig. 2(a), which was divided into: brain, skull, and muscle, with different empirical optical parameters listed in Section B of the supplementary material. Homogeneous density of 1 nw/mm^3 was used in each source, and the molecular optical simulation environment (MOSE) was used to simulate the surface flux distribution with the Monte Carlo method [35] as shown in Fig. 2(c) (spherical source, cylindrical source, and dual-source). In addition, 10% additive Gaussian noise was added to the surface measurements to mimic measurement uncertainty and the inevitable presence of noise. For the inverse reconstruction, the digital mouse model was discretized into a uniform tetrahedral mesh (Fig. 2(b)) including 11,018 nodes and 61,699 tetrahedral elements. The performance of each algorithm was quantified using the quantitative analysis index position error (PE) and the Dice similarity coefficient, which were listed in Section C of the supplementary material.

1) Feasibility verification: To evaluate the feasibility of our proposed method, we performed a series of tests with different combinations of parameters (error variance λ and group size K). A spherical source (radius: 1 mm, spatial position of x-, y- and z-axis: 13 mm, 19.5 mm, 14 mm) was applied for the simulation as an example. λ was set to 0.1, 1, 5, 10, 15, 20, and 50, whereas K was set to 5, 15, 25, 35, 50, 75, and 100. Quantitative comparisons of PE and Dice for KNN-BSBL with different λ and K were plotted in Fig. 3(a). The same method was used to test the parameters of KNN-GBSBL and the quantitative comparisons were shown in Fig. 3(b).

These results indicated that, as with the KNN-BSBL, both PE and Dice became stable when K ranged from 15 to 100. However, reconstruction accuracy increased with decreasing λ, until the value of λ became equal to one. KNN-GBSBL can accurately reconstruct sources, especially for K values of 25–100 and λ values of 10–50. According to the results, we used the K = 15, $\lambda = 1$ for KNN-BSBL and K = 75, $\lambda = 20$ for KNN-GBSBL, respectively.

The parameters employed for SBR ($a = 1$, $b = 10^4$) and GWLP ($\lambda = 0.1$) were also optimized according to their relevant protocols [5], [19]. Moreover, as GWLP required a threshold of the optical intensity scale for visualization and quantification [19], whereas all other methods did not, we applied two scale bars (0.45 to 1 for GWLP and 0 to 1 for the other methods) in the remainder of our comparisons.

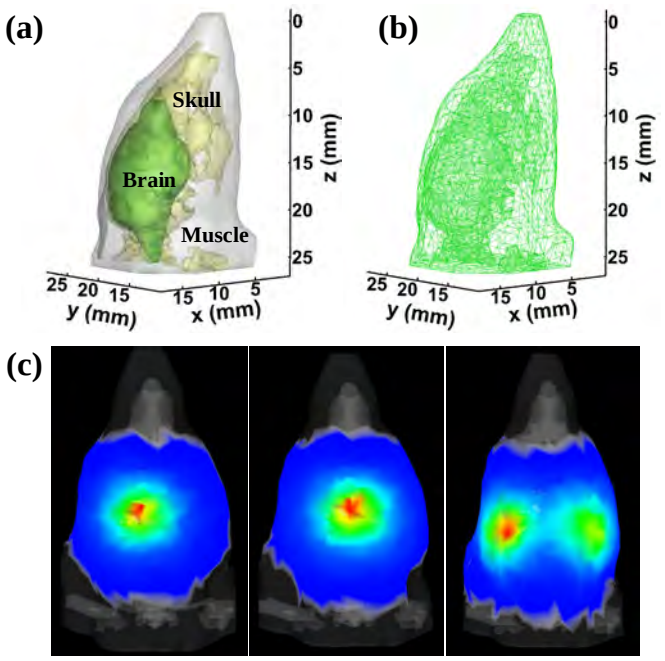

Fig. 2. Numerical simulation settings. (a) The head of digital mouse model; (b) The uniform tetrahedral mesh used in reconstruction. (c) The surface flux distribution with the Monte Carlo method (spherical source, cylindrical source, and dual-source).

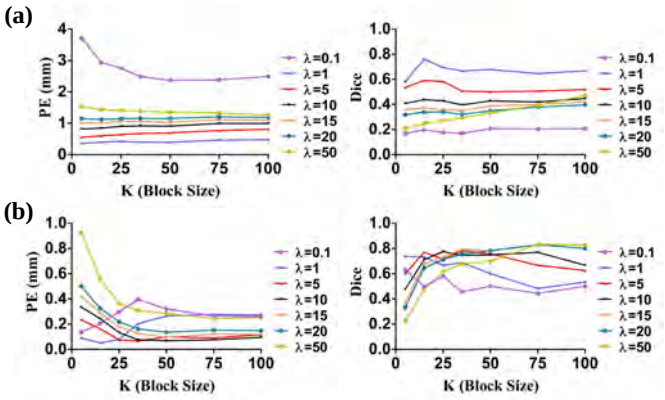

Fig. 3. Spherical source reconstructions by KNN-BSBL and KNN-GBSBL with different λ and K: (a) PE and Dice profile curves using different λ and K for KNN-BSBL. (b) PE and Dice profile curves using different λ and K for KNN-GBSBL

2) Single source simulations: The spherical source phantom mentioned above as well as a cylindrical source phantom (radius: 1 mm, height: 2 mm, spatial position of the x-, y- and z-axis: 12.5 mm, 19.0 mm, 14.5 mm) was applied to evaluate the performance of the BLT reconstruction. The results were shown in Fig. 4. In spherical source simulation, the depth of the tumor was approximately 2.8 mm. The quantitative analysis (Table I) revealed that SBR reconstruction achieved good positioning accuracy but was limited by over-sparsity. The positioning accuracy of GWLP was worst and

This article has been accepted for publication in a future issue of this journal, but has not been fully edited. Content may change prior to final publication. Citation information: DOI 10.1109/TBME.2019.2953732, IEEE Transactions on Biomedical Engineering

the reconstruction result was very shallow and smooth. KNN-BSBL achieved a more accurate result than SBR and GWLP in terms of morphology. Moreover, PE and Dice of KNN-GBSBL were superior to that of KNN-BSBL. The tumor deepened in depth (approximately 3.5 mm) in cylindrical source simulation. According to the results of quantitative analysis (Table I), we found that positioning accuracy of SBR was greatly reduced, and it still showed over-sparsity. GWLP did not accurately locate the tumor and also show smoothness. KNN-BSBL was superior than SBR and GWLP in both positioning and morphology. In addition, KNN-GBSBL exhibited the best reconstruction, which had the largest overlap with the real source.

3) Dual-source simulation: We further compared the BLT reconstruction performance of each method for multiple sources. We set two sources with the same size (radius = 1 mm) in two locations inside the digital mouse brain (x-y-z: 13.0 mm, 16.0 mm, 16.0 mm, and 13.0 mm, 22.0 mm, 16.0 mm) (The depth was approximately 2.8 mm). The results shown in Fig. 5 were similar to those of the single source simulations. SBR had high positioning accuracy but exhibited substantial over-sparsity. GWLP showed significantly lower spatial resolution and only one of the tumors was correctly reconstructed. Conversely, KNN-BSBL achieved much better results than SBR and GWLP in terms of morphology. KNN-GBSBL still provided the best reconstruction in terms of positioning and morphological recovery (Table I).

TABLE I
QUANTITATIVE ANALYSIS OF NUMERICAL SIMULATION RESULTS FOR FOUR BLT RECONSTRUCTION METHODS

Case	Indexes	SBR	GWLP	KNN-BSBL	KNN-GBSBL
Spherical source	PE (mm)	0.19	0.63	0.31	**0.15**
	Dice	0.09	0.6	0.73	**0.83**
Cylindrical source	PE (mm)	0.73	1.19	0.32	**0.27**
	Dice	0.07	0.32	0.60	**0.64**
Dual-source	PE1 (mm)	0.12	1.77	0.22	**0.11**
	PE2 (mm)	0.28	0.77	0.07	**0.05**
	Dice1	0.1	0	0.55	**0.82**
	Dice2	0.15	0.50	0.7	**0.79**

B. in vivo Experiments

All animal experiments were conducted under the approval of the Institutional Animal Care and Use Committee of the Chinese Academy of Sciences. Three female BALB/c nude mice (6–8 weeks old) were provided by the Peking University Laboratory Animal Center and used to establish orthotopic glioma mouse models with a conventional protocol [36]. The details of the data acquisition and the experimental procedure are described in Section D of the supplementary material.

PE and Dice were also calculated in *in vivo* experiments. We merged the H&E images with the corresponding axil slices firstly based on the "imregister" function of MATLAB. Then, we calculated the tumor barycenter and the tumor area given by H&E image and by our reconstruction method, respectively. Moreover, the area of overlapped tumor region between the H&E image and the reconstructed image was also calculated. After these, the PE and Dice index were calculated according to the supplemental Eq. (5) and (6), which were listed in Section C of the supplementary material. The performance of all four BLT reconstruction methods on real glioma-bearing mice data was relatively consistent with the data obtained from the simulations with digital mice (Fig. 6). The PE and dice coefficients were compared in Table II. The SBR results were characterized by over-sparsity and the location was considerably far from the target in Mouse 1. GWLP achieved over-smooth results and a systematic tendency to overly restore the tumor region in the horizontal direction, whereas reconstruction in the vertical direction was inadequate. In comparison, the tumor reconstruction performance of KNN-BSBL and KNN-GBSBL was superior for all three mice because the reconstructed tumors predominantly overlapped with the pathologically defined tumor regions. A quantitative analysis further validated our observations (Table II). In Mouse 1, KNN-GBSBL achieved the best results. In Mouse 2 and Mouse 3, both KNN-BSBL and KNN-GBSBL achieved similar excellent performance.

TABLE II
QUANTITATIVE ANALYSIS OF THE IN VIVO EXPERIMENTS FOR THE FOUR BLT RECONSTRUCTION METHODS

Case	Indexes	SBR	GWLP	KNN-BSBL	KNN-GBSBL
Mouse 1	PE (mm)	0.93	0.37	0.23	**0.22**
	Dice	0	0.7	0.72	**0.75**
Mouse 2	PE (mm)	**0.11**	0.31	0.2	0.22
	Dice	0.1	0.64	0.66	**0.67**
Mouse 3	PE (mm)	0.42	0.28	**0.23**	0.28
	Dice	0.34	0.73	0.75	**0.76**

IV. DISCUSSION

In this study, we proposed a KNN-BSBL method for the BLT reconstruction to trace the bioluminescent source location and the source morphology in 3D. The results in numerical simulations and *in vivo* experiments demonstrated that the proposed method achieved the best accuracy and morphology recovery compared with SBR and GWLP. Furthermore, we also proposed the KNN-GBSBL method to improve the intra-block correlation matrix and enhance the performance of KNN-BSBL.

In terms of algorithm design, considering that the light source of BLT is clustered in space, we can solve the inverse problem under the BSBL framework to further exploit the structural characteristics. However, during the data processing of BLT, we need to discretize CT data into a grid under the FEM framework. Further, this discretization is unordered such that the traditional BSBL algorithm cannot be directly applied to solve the BLT problem. Therefore, in this study we proposed a KNN-BSBL method that helped design a block sparse prior model utilizing the sparsity and spatial correlations among neighboring points of light source based

This article has been accepted for publication in a future issue of this journal, but has not been fully edited. Content may change prior to final publication. Citation information: DOI 10.1109/TBME.2019.2953732, IEEE Transactions on Biomedical Engineering

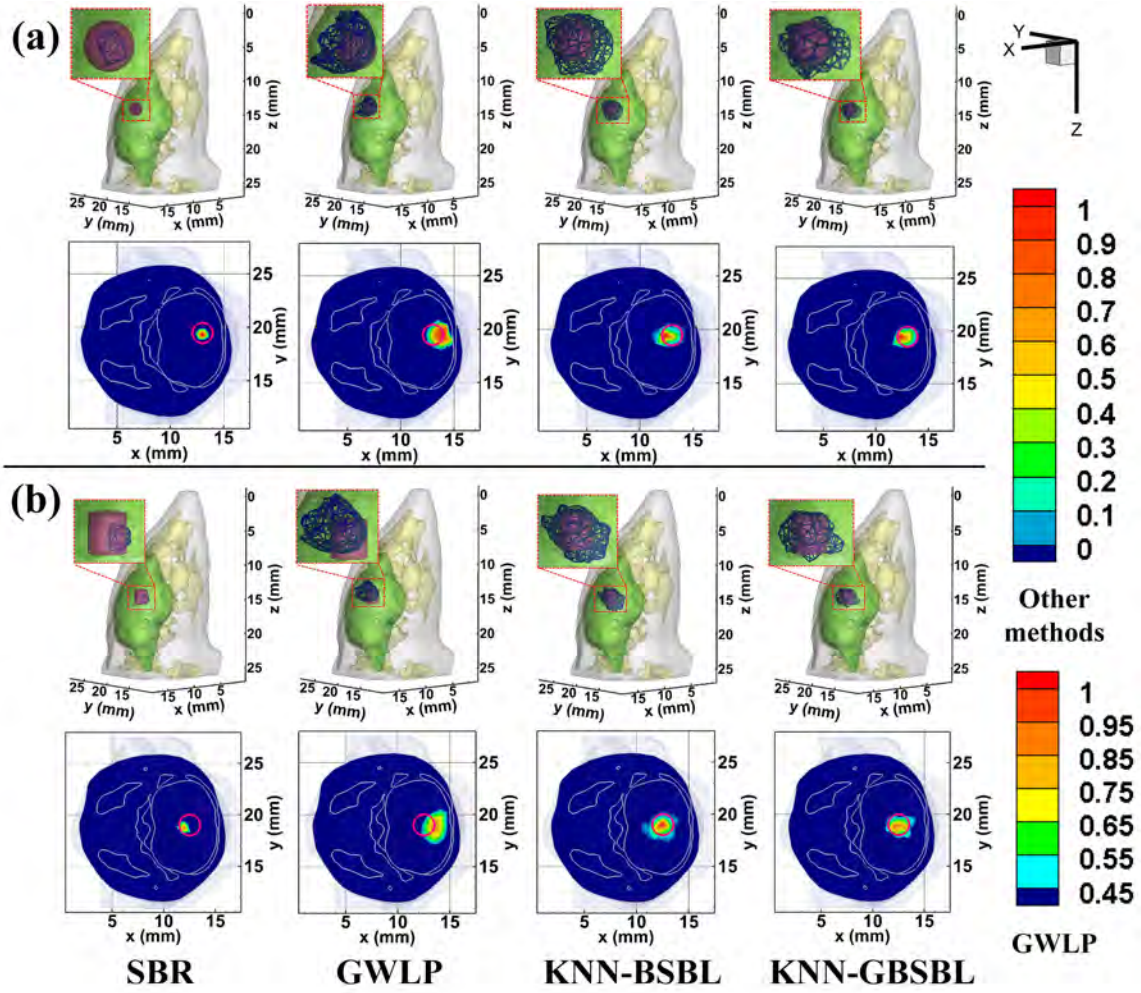

Fig. 4. Reconstruction comparisons for the single light source. (a) 3D rendering and 2D tomographic slices (z = 14mm) of the spherical source phantom. (b) 3D rendering and 2D tomographic slices (z = 14.5mm) of the cylindrical source phantom. The red outline indicates the real source location and shape.

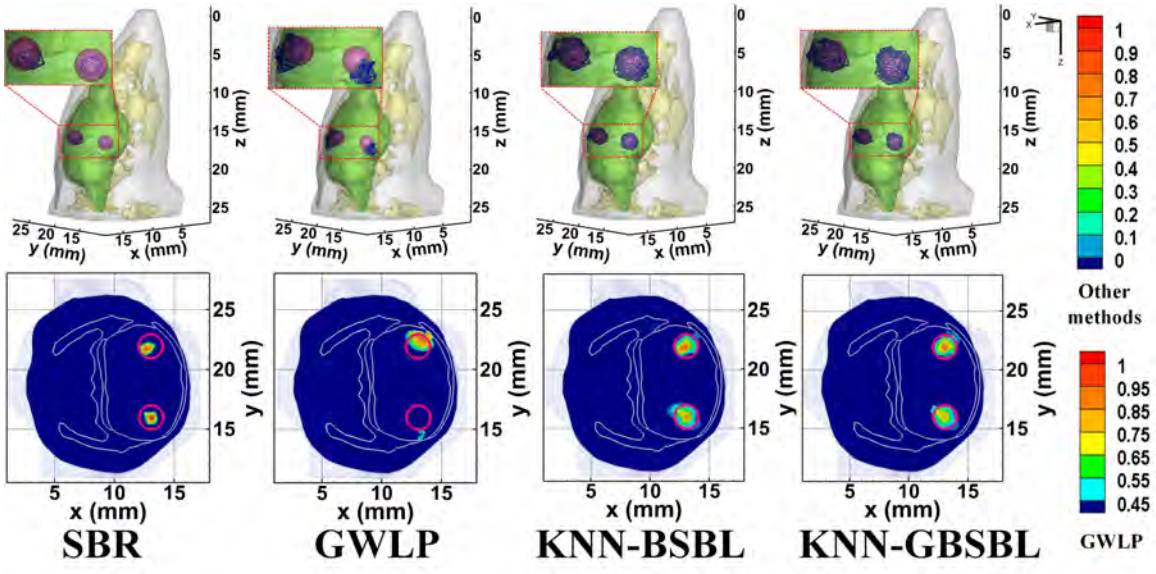

Fig. 5. Reconstruction comparisons for the dual-source. 3D rendering and a selected 2D tomographic slice (z = 16mm) in the transverse view are demonstrated for comparison. The red outline indicates the location and shape of two real sources.

This article has been accepted for publication in a future issue of this journal, but has not been fully edited. Content may change prior to final publication. Citation information: DOI 10.1109/TBME.2019.2953732, IEEE Transactions on Biomedical Engineering

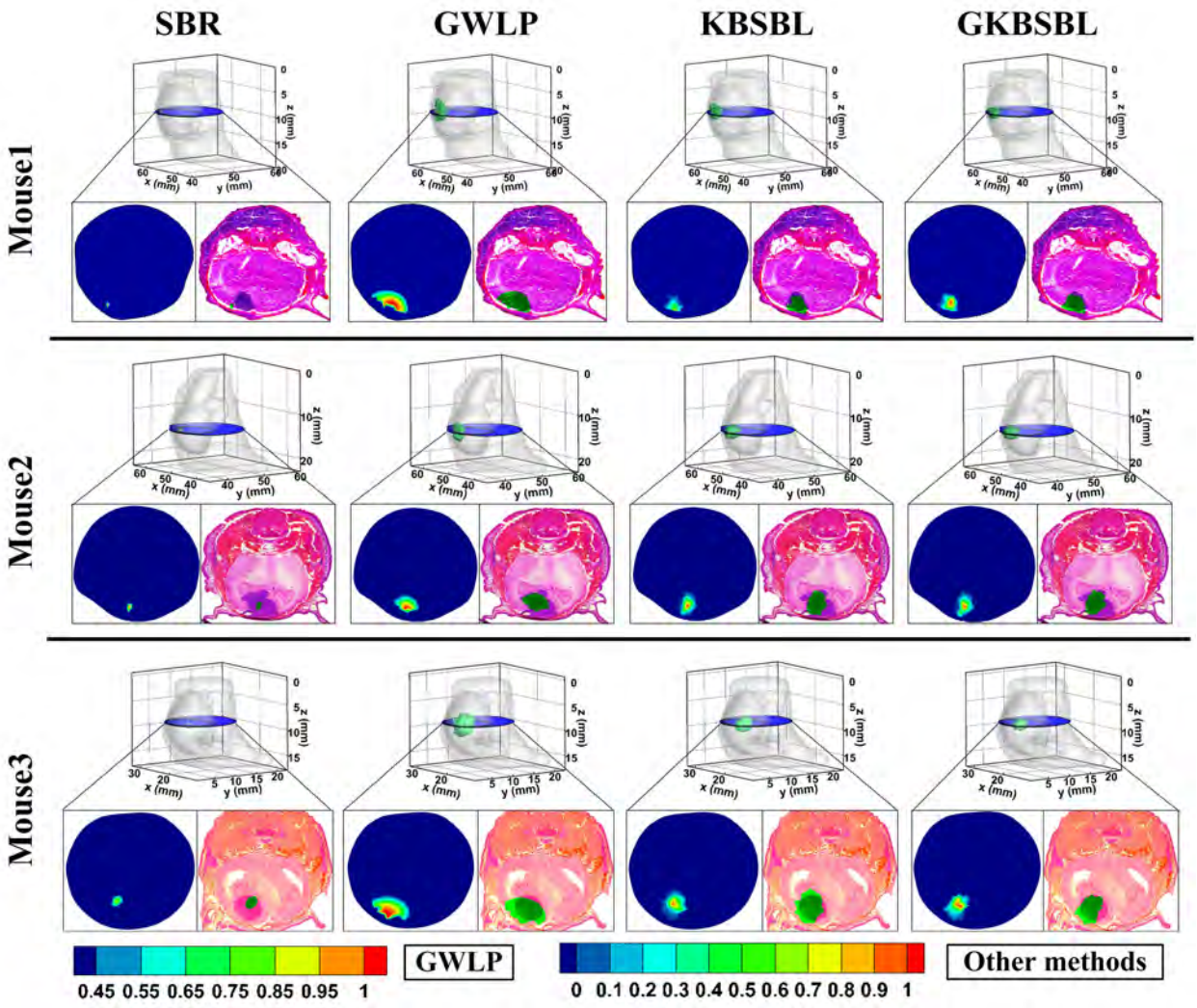

Fig. 6. Results of *in vivo* experiments of three orthotopic glioma-bearing mouse models. Comparison of glioma reconstructions between the four methods, as well as between *in vivo* BLT images (3D rendering and 2D tomographic slices in transverse view) and their corresponding *ex vivo* pathological images.

on the KNN strategy, and then solved the inverse problem under the BSBL framework. Each point on the grid is not isolated from its neighborhood, however, substituted by its corresponding group to overcome over-sparsity. The biggest advantage of KNN-BSBL is that the combination of various a priori information including sparsity, spatial neighborhood correlations, and anatomical structure helps balance the sparsity and morphology recovery. Moreover, we also proposed an improved algorithm KNN-GBSBL, considering the Gaussian weighted distance prior [19] to improve the intra-block correlation matrix. This strategy simplified the computational complexity and enhanced the performance of KNN-BSBL. This proved that under the Bayesian framework, combining more accurate a priori information to design the solution strategy can improve the reconstruction performance of the strategy.

The KNN-BSBL and KNN-GBSBL strategies were thoroughly validated using both numerical simulations and *in vivo* glioma-bearing mouse models. Two existing reconstruction methods (SBR and GWLP) were compared to evaluate the accuracy of tumor location and morphology reconstruction. All digital mouse simulations, including single- and dual-source experiments, demonstrated very consistent results. KNN-BSBL exhibited the highest accuracy when restoring the morphology of the bioluminescence source in all experiments compared with SBR and GWLP. KNN-GBSBL improves the performance of KNN-BSBL by eliminating a few reconstruction artifacts. In spherical source simulations, SBR achieved the superior positioning accuracy; however, when the tumor shape varied and depth deepened (cylindrical source simulations), the performance of SBR and GWLP was considerably reduced. The performance of KNN-BSBL and KNN-GBSBL also declined slightly; however, it was still significantly superior than SBR and GWLP. The results of dual-source simulation were consistent with that of the single source, whereas GWLP exhibited the worst performance with considerably low spatial resolution. The maximum PEs of KNN-BSBL and KNN-GBSBL were consistently less than 0.32 mm. Considering that the tumor size is typically several mm to 1 cm in *in vivo* applications, this level of

barycenter positioning error is almost negligible. Therefore, as multiple methods exhibited similar PE values, their ability to reconstruct tumor morphology was sued to distinguish their relative performance. The *in vivo* experiments further proved the superiority of KNN-BSBL and KNN-GBSBL over their competitors. After projecting the reconstructed tumor region into the ultimate gold standard, H&E stained pathological images, it was clear that KNN-BSBL and KNN-GBSBL achieved evidently accurate BLT reconstructions in all three mice. The performance of SBR was considerably low to draw a meaningful comparison. Moreover, GWLP exhibited a systematic tendency to overly restore the tumor region in the horizontal direction and smoothness.

SBR is a type of sparse Bayesian method designed to achieve accurate positioning, considering solely the sparsity of the light source. Our experimental results also demonstrated that SBR had high positioning accuracy but exhibited substantial over-sparsity. The general effectiveness of GWLP for tumor morphological reconstruction has already been proved [19]. In that study, the multispectral strategy was used to improve the reconstructed accuracy including spatial resolution. However, in order to evaluate the reconstruction performance of our proposed method and make comparisons with referenced methods in a more challengeable situation, we did not apply the multispectral strategy for all methods. Our results demonstrated that without multispectral information, GWLP suffered from biased reconstruction and smoothness in the horizontal direction, thereby revealing a major weakness of GWLP. Although it was designed to restore tumor morphology as much as possible, it still employed an L2-norm regularization-based approach. To reduce the over-smoothness, it utilized a threshold of the normalized optical intensity scale (≥ 0.45). This led to different reconstruction behavior in different scenarios, which limited the applicability of GWLP for small animals. In contrast to GWLP, KNN-BSBL achieved a good balance between over-sparsity and over-smoothness without using any mandatory preset threshold. This unique capability ensures various and robust applications of KNN-BSBL. The overall results of KNN-GBSBL were better than those of KNN-BSBL; this indicates that the use of Gaussian weighted distance prior strategy not only simplified the calculation process, but also enhanced the performance of reconstruction. This improvement of intra-block correlation matrix also provided a research direction to improve the BSBL algorithm in the future.

Nonetheless, there are two major limitations of the proposed KNN-BSBL strategy. First, as with the majority of BLT reconstruction methods, it still requires an optimization process when selecting the parameters (the error variance λ and the group size K). If K exceeds a certain threshold, it has a slight effect on the results. This is because the neighboring points that have a large influence on the center point are those that are close to it; those that are far away have a relatively small influence; thus, the result will not be considerably affected by increasing the value of K. λ is related to the model error; thus, it may vary under different experimental conditions. This could lead to multiple parameter selection processes for different tumor types besides glioma, such as liver cancer and lung cancer. Second, KNN-BSBL increases the computational time by implementing the expanding rule used in the prior model. However, we believe that these two issues can be solved in out further work. Moreover, all experiments in this study were based on single spectrum (620 nm); hence, our future research will also consider introducing a multispectral strategy to further improve reconstruction performance.

V. Conclusion

This paper proposed a block sparse Bayesian learning method using KNN strategy (KNN-BSBL) utilizing sparsity, spatial correlation among neighboring points, and an anatomical structure to achieve accurate and practical BLT reconstruction of tumor location and morphology. This unique design allowed BLT reconstruction to overcome the limitations of over-sparsity without leading to smooth reconstruction results. Both numerical simulations and *in vivo* glioma-bearing mouse models revealed that the KNN-BSBL can achieve accurate and robust BLT reconstruction of glioma location and morphology by inheriting the benefits of both structural a priori regularization and the sparse regularization approach. We believe that this novel strategy has substantial significance in biomedical engineering as it can facilitate the application of BLT to quantitative observations of various tumor-bearing mouse models, and it can be applicable to the related optical tomography. In addition, it will bring many benefits to pre-clinical applications and will also promote theoretical research on optical tomography.

References

[1] V. Ntziachristos *et al.*, "Looking and listening to light: the evolution of whole-body photonic imaging," *Nature biotechnology*, vol. 23, no. 3, p. 313, 2005.

[2] G. Wang *et al.*, "Uniqueness theorems in bioluminescence tomography," *Medical physics*, vol. 31, no. 8, pp. 2289–2299, 2004.

[3] H. Guo *et al.*, "A hybrid clustering algorithm for multiple-source resolving in bioluminescence tomography," *Journal of biophotonics*, vol. 11, no. 4, p. e201700056, 2018.

[4] T. F. Massoud *et al.*, "Molecular imaging in living subjects: seeing fundamental biological processes in a new light," *Genes & development*, vol. 17, no. 5, pp. 545–580, 2003.

[5] J. Feng *et al.*, "Bayesian sparse-based reconstruction in bioluminescence tomography improves localization accuracy and reduces computational time," *Journal of biophotonics*, vol. 11, no. 4, p. e201700214, 2018.

[6] X. Zhang *et al.*, "A novel sparsity reconstruction method from poisson data for 3d bioluminescence tomography," *Journal of scientific computing*, vol. 50, no. 3, pp. 519–535, 2012.

[7] X. He *et al.*, "Sparse reconstruction for quantitative bioluminescence tomography based on the incomplete variables truncated conjugate gradient method," *Optics Express*, vol. 18, no. 24, pp. 24 825–24 841, 2010.

[8] J. Yu *et al.*, "Systematic study of target localization for bioluminescence tomography guided radiation therapy," *Medical physics*, vol. 43, no. 5, pp. 2619–2629, 2016.

[9] M. A. Naser *et al.*, "Algorithms for bioluminescence tomography incorporating anatomical information and reconstruction of tissue optical properties," *Biomedical optics express*, vol. 1, no. 2, pp. 512–526, 2010.

[10] H. Gao *et al.*, "Bioluminescence tomography with gaussian prior," *Biomedical optics express*, vol. 1, no. 5, pp. 1259–1277, 2010.

[11] S. Jiang *et al.*, "Novel l 2, 1-norm optimization method for fluorescence molecular tomography reconstruction," *Biomedical optics express*, vol. 7, no. 6, pp. 2342–2359, 2016.

[12] Y. Lv *et al.*, "A multilevel adaptive finite element algorithm for bioluminescence tomography," *Optics Express*, vol. 14, no. 18, pp. 8211–8223, 2006.

[13] C. Qin *et al.*, "Comparison of permissible source region and multispectral data using efficient bioluminescence tomography method," *Journal of biophotonics*, vol. 4, no. 11-12, pp. 824–839, 2011.

[14] K. Wang *et al.*, "Optical molecular imaging frontiers in oncology: the pursuit of accuracy and sensitivity," *Engineering*, vol. 1, no. 3, pp. 309–323, 2015.

[15] A. D. Klose, *et al.*, "In vivo bioluminescence tomography with a blocking-off finite-difference method and mri/ct coregistration," *Medical physics*, vol. 37, no. 1, pp. 329–338, 2010.

[16] Y. Lv *et al.*, "Spectrally resolved bioluminescence tomography with adaptive finite element analysis: methodology and simulation," *Physics in Medicine & Biology*, vol. 52, no. 15, p. 4497, 2007.

[17] S. C. Davis *et al.*, "Comparing implementations of magnetic-resonance-guided fluorescence molecular tomography for diagnostic classification of brain tumors," *Journal of biomedical optics*, vol. 15, no. 5, p. 051602, 2010.

[18] S. C. Davis *et al.*, "Dynamic dual-tracer mri-guided fluorescence tomography to quantify receptor density in vivo," *Proceedings of the National Academy of Sciences*, vol. 110, no. 22, pp. 9025–9030, 2013.

[19] Y. Gao *et al.*, "Bioluminescence tomography based on gaussian weighted laplace prior regularization forin vivomorphological imaging of glioma," *IEEE transactions on medical imaging*, vol. 36, no. 11, pp. 2343–2354, 2017.

[20] C. Chen *et al.*, "Diffuse optical tomography enhanced by clustered sparsity for functional brain imaging," *IEEE transactions on medical imaging*, vol. 33, no. 12, pp. 2323–2331, 2014.

[21] S. Jiang *et al.*, "Reconstruction of fluorescence molecular tomography via a fused lasso method based on group sparsity prior," *IEEE Transactions on Biomedical Engineering*, vol. 66, no. 5, pp. 1361–1371, 2018.

[22] G. Zhang *et al.*, "Map estimation with structural priors for fluorescence molecular tomography," *Physics in Medicine & Biology*, vol. 58, no. 2, p. 351, 2012.

[23] Z. Zhang *et al.*, "Extension of sbl algorithms for the recovery of block sparse signals with intra-block correlation," *IEEE Transactions on Signal Processing*, vol. 61, no. 8, pp. 2009–2015, 2013.

[24] M. Schweiger *et al.*, "The finite element method for the propagation of light in scattering media: boundary and source conditions," *Medical physics*, vol. 22, no. 11, pp. 1779–1792, 1995.

[25] G. Wang *et al.*, "In vivo mouse studies with bioluminescence tomography," *Optics Express*, vol. 14, no. 17, pp. 7801–7809, 2006.

[26] J. C. Ye *et al.*, "Optical diffusion tomography by iterative-coordinate-descent optimization in a bayesian framework," *JOSA A*, vol. 16, no. 10, pp. 2400–2412, 1999.

[27] G. Zhang *et al.*, "Cone beam x-ray luminescence computed tomography based on bayesian method," *IEEE transactions on medical imaging*, vol. 36, no. 1, pp. 225–235, 2016.

[28] J. M. Keller *et al.*, "A fuzzy k-nearest neighbor algorithm," *IEEE transactions on systems, man, and cybernetics*, no. 4, pp. 580–585, 1985.

[29] Y. C. Eldar *et al.*, "Robust recovery of signals from a structured union of subspaces," *IEEE Transactions on Information Theory*, vol. 55, no. 11, pp. 5302–5316, 2009.

[30] Z. Zhang *et al.*, "Sparse signal recovery with temporally correlated source vectors using sparse bayesian learning," *IEEE Journal of Selected Topics in Signal Processing*, vol. 5, no. 5, pp. 912–926, 2011.

[31] M. E. Tipping, "Sparse bayesian learning and the relevance vector machine," *Journal of machine learning research*, vol. 1, no. Jun, pp. 211–244, 2001.

[32] S. D. Babacan *et al.*, "Bayesian group-sparse modeling and variational inference," *IEEE transactions on signal processing*, vol. 62, no. 11, pp. 2906–2921, 2014.

[33] S. Ji *et al.*, "Bayesian compressive sensing," *IEEE Transactions on signal processing*, vol. 56, no. 6, p. 2346, 2008.

[34] B. Dogdas *et al.*, "Digimouse: a 3d whole body mouse atlas from ct and cryosection data," *Physics in Medicine & Biology*, vol. 52, no. 3, p. 577, 2007.

[35] N. Ren *et al.*, "Gpu-based monte carlo simulation for light propagation in complex heterogeneous tissues," *Optics express*, vol. 18, no. 7, pp. 6811–6823, 2010.

[36] M. F. Kircher *et al.*, "A brain tumor molecular imaging strategy using a new triple-modality mri-photoacoustic-raman nanoparticle," *Nature medicine*, vol. 18, no. 5, p. 829, 2012.